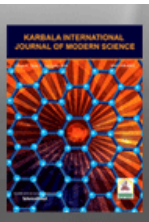

Karbala International Journal of Modern Science

Volume 12 | Issue 2 Article 11

High-surface-area Ficus leaf-extracted CuO-ZnO-NiO ternary nanocomposites for rapid adsorption-assisted UV-A degradation of Direct Blue 15

Kafa'a H. Ali
Department of Biochemical Engineering, Al-Khwarizmi College of Engineering, University of Baghdad, Baghdad, Iraq;,
Kafaahali@gmail.com

Mohammed A. Atiya
Department of Biochemical Engineering, Al-Khwarizmi College of Engineering, University of Baghdad, Baghdad, Iraq;

Ahmed K. Hassan
Scientific Research Commission, Research and Technology Center of Environment, Water and Renewable Energy, Baghdad, Iraq.

High-surface-area Ficus leaf-extracted CuO-ZnO-NiO ternary nanocomposites for rapid adsorption-assisted UV-A degradation of Direct Blue 15

Abstract

Direct Blue 15 (DB15) is a long-lasting synthetic dye that pollutes water and is difficult to remove during wastewater treatment. Conventional treatments fail to remove DB15 adequately due to rapid electron-hole recombination, which necessitates photocatalysts with reduced recombination rates for effective dye removal. The study aims to synthesize and evaluate a CuO-ZnO-NiO ternary system as an integrated adsorption and UV-A photocatalysis platform for DB15 removal. *Ficus* leaf-extracted CuO-ZnO-NiO nanocomposites with four Cu:Zn:Ni ratios (1:1:1, 1:1:2, 1:2:1, 2:1:1) were prepared by co-precipitation, followed by extensive chemical and physical characterization and dye-removal performance measurements. The CuO-ZnO-NiO nanocomposite exhibited hexagonal zinc oxide, cubic nickel oxide, and monoclinic copper oxide phases, with mixed morphologies and a mean particle size of 56.75 nm. The nanocomposite had a specific surface area of 34.741 $m^2 g^{-1}$ and a total pore volume of 0.089 $cm^3 g^{-1}$. Among the four ratios, the 1:1:1 Cu:Zn:Ni nanocomposite delivered the highest overall performance, achieving complete DB15 removal by adsorption at 20 mg L^{-1} and complete DB15 degradation by UV-A photocatalysis at 30 mg L^{-1}, both within 150 min. Reuse tests of the nanocomposite over five consecutive cycles yielded DB15 degradation efficiencies of 95%, 93%, 91%, 63%, and 59%. Kinetic and equilibrium analyses indicated pseudo-second-order behaviour and Langmuir-type adsorption, and thermodynamic parameters indicated a spontaneous, endothermic adsorption process. *Ficus*-based CuO-ZnO-NiO nanocomposites enable high DB15 degradation through complementary adsorption and UV-A photocatalytic pathways and support practical wastewater treatment applications.

Keywords

Photocatalysis; Green Synthesis; CuO-ZnO-NiO Ternary Metal Oxide Nanocomposites; Adsorption; Kinetic Model-ling.

RESEARCH PAPER

High-surface-area *Ficus* Leaf-extracted CuO-ZnO-NiO Ternary Nanocomposites for Rapid Adsorption-assisted UV-A Degradation of Direct Blue 15

Kafa'a H. Ali [a,*], Mohammed A. Atiya [a], Ahmed K. Hassan [b]

[a] Department of Biochemical Engineering, Al-Khwarizmi College of Engineering, University of Baghdad, Baghdad, Iraq
[b] Scientific Research Commission, Research and Technology Center of Environment, Water and Renewable Energy, Baghdad, Iraq

Abstract

Direct Blue 15 (DB15) is a long-lasting synthetic dye that pollutes water and is difficult to remove during wastewater treatment. Conventional treatments fail to remove DB15 adequately due to rapid electron-hole recombination, which necessitates photocatalysts with reduced recombination rates for effective dye removal. The study aims to synthesize and evaluate a CuO-ZnO-NiO ternary system as an integrated adsorption and UV-A photocatalysis platform for DB15 removal. *Ficus* leaf-extracted CuO-ZnO-NiO nanocomposites with four Cu:Zn:Ni ratios (1:1:1, 1:1:2, 1:2:1, 2:1:1) were prepared by co-precipitation, followed by extensive chemical and physical characterization and dye-removal performance measurements. The CuO-ZnO-NiO nanocomposite exhibited hexagonal zinc oxide, cubic nickel oxide, and monoclinic copper oxide phases, with mixed morphologies and a mean particle size of 56.75 nm. The nanocomposite had a specific surface area of 34.741 $m^2\ g^{-1}$ and a total pore volume of 0.089 $cm^3\ g^{-1}$. Among the four ratios, the 1:1:1 Cu:Zn:Ni nanocomposite delivered the highest overall performance, achieving complete DB15 removal by adsorption at 20 mg L^{-1} and complete DB15 degradation by UV-A photocatalysis at 30 mg L^{-1}, both within 150 min. Reuse tests of the nanocomposite over five consecutive cycles yielded DB15 degradation efficiencies of 95%, 93%, 91%, 63%, and 59%. Kinetic and equilibrium analyses indicated pseudo-second-order behaviour and Langmuir-type adsorption, and thermodynamic parameters indicated a spontaneous, endothermic adsorption process. *Ficus*-based CuO-ZnO-NiO nanocomposites enable high DB15 degradation through complementary adsorption and UV-A photocatalytic pathways and support practical wastewater treatment applications.

Keywords: Photocatalysis, Green synthesis, CuO-ZnO-NiO ternary metal oxide nanocomposites, Adsorption, Kinetic modelling

1. Introduction

Water pollution is a growing threat to aquatic ecosystems and public health. In many regions, industrial and municipal sources discharge large volumes of inadequately treated wastewater into natural waters, which can contain contaminants such as dyes, pharmaceuticals, heavy metals, and pathogenic microorganisms [1,2]. Industries such as textile, plastic, tanning, paper, and leather are major contributors to dye-laden effluents in rivers and lakes, where persistent dyes reduce water quality and harm aquatic life by blocking light penetration and inducing ecological toxicity [1].

Direct Blue 15 (DB15) is a benzidine-based diazo dye used extensively in textile, leather, and paper manufacture [3]. DB15 enters aquatic systems

Received 23 January 2026; revised 3 April 2026; accepted 7 April 2026.
Available online 13 May 2026

* Corresponding author.
E-mail address: kafaahali@gmail.com (K.H. Ali).

https://doi.org/10.33640/2405-609X.3463

through industrial wastewater discharge, and dye-processing lines release up to 10% of applied dyes into effluents. Its aromatic diazo structure gives DB15 high chemical stability and poor biodegradability, so conventional wastewater treatment often fails to remove it completely. DB15 poses risks across multiple trophic levels [4]. Hernández-Zamora and Martínez-Jerónimo (2019) reported stunted growth in freshwater microalgae, reduced reproduction in cladocerans, and developmental abnormalities in zebrafish larvae after DB15 exposure [5].

Conventional wastewater treatment routes rely on adsorption, filtration, coagulation-flocculation, chemical oxidation, and reverse osmosis. However, many conventional removal methods shift pollutants between phases rather than performing a complete removal [6]. Adsorption-based removal can concentrate dyes onto solid sorbents, and membrane separation can concentrate contaminants into retentate streams. Both approaches create secondary waste streams that require additional handling and disposal [6,7]. Conventional chemical treatments can also introduce operational limitations through reagent costs and by-product risks. Besides, several dye classes resist complete removal within standard treatment trains because dye structures remain stable under mild conditions [2].

Advanced oxidation processes offer a more effective alternative because reactive oxygen species, particularly hydroxyl radicals (·OH) and superoxide radicals ($O_2\cdot-$), can break down a broad range of organic pollutants into harmless mineral end products [8]. Semiconductor photocatalysis is one of the most widely studied advanced oxidation processes, in which light excitation generates electron-hole pairs that produce radicals at the catalyst surface [2]. However, photocatalytic efficiency is often limited by rapid electron-hole recombination and by the inability of wide-band-gap oxides to absorb visible light, as their response is mainly to ultraviolet wavelengths, which represent only a small fraction of solar radiation [9]. Composite catalysts can mitigate these barriers when heterojunction interfaces promote charge separation through built-in electric fields, which reduces recombination and improves reaction rates. Binary oxide nanocomposites often exploit this principle. Interestingly, higher photocatalytic degradation rates were reported for paired oxides, as interfacial charge separation becomes more efficient due to the dual effect [6].

Nanomaterials play a key role in many modern technologies, including biomedical imaging, fuel cells, batteries, sensors, energy storage, and optical devices [10]. Metal oxides nanomaterials, such as zinc oxide (ZnO) [11], titanium dioxide (TiO_2) [12], nickel(II) oxide (NiO) [13], copper(II) oxide (CuO) [14], and doped metal oxides [15] are widely used and have been evaluated for photodegradation of hazardous organic contaminants [16]. Binary and ternary metal oxide systems have shown good performance in several cases. For instance, a binary metal oxide system of ZnO-MgO has demonstrated enhanced antibacterial and photocatalytic activity [17], and a ternary metal oxide system of ZnO-MgO-TiO_2 has shown photocatalytic activity [18].

ZnO functions as a widely used n-type semiconductor that offers low cost, low toxicity, and a band structure that supports radical generation under ultraviolet illumination, and ZnO synthesis permits morphology control across nanoparticles and nanorods that suit water treatment applications [19]. ZnO also maintains chemical stability under ultraviolet irradiation, yet ZnO suffers from electron-hole recombination and photo-corrosion, which limit quantum efficiency in single-oxide form. CuO is a p-type semiconductor with a narrower band gap (approximately 1.2-1.9 eV) and stronger absorption across visible and near-infrared wavelengths, extending photoactivity beyond ultraviolet excitation [20]. CuO can also form a p-n junction with n-type ZnO, and p-n junction formation can promote charge separation. Although CuO itself can experience charge recombination in isolation, it is expected to slightly extend light absorption into the visible range due to its narrower band gap relative to ZnO and NiO [21]. NiO represents a p-type oxide with a wide band gap (approximately 3.5-4.0 eV at the nanoscale), and NiO contributes high chemical stability and effective hole-acceptor function in heterojunction composites rather than visible absorption [22]. NiO ionic character supports repeated redox cycling with limited photo-corrosion, and NiO hole acceptance reduces hole-electron recombination at an n-type partner interface, which extends charge-carrier lifetime and increases oxidative radical generation [23].

ZnO-NiO heterostructures have shown higher methylene blue degradation than either ZnO or NiO alone, and under the reported conditions, achieved about 70% dye removal, which the authors attributed to an internal electric field that promotes charge separation [24]. ZnO-CuO composites also exhibit enhanced visible-light activity and antimicrobial effects, and reports commonly attribute these gains to CuO's visible absorption and ZnO's surface reactivity at a coupled interface [25,26].

Ishaque *et al.* (2023) reported that ZnO-NiO-CuO nanocomposites with tuned metal ratios achieved higher photocatalytic efficiency when all three oxides coexisted within the composite and reported around 98% methylene blue degradation and around 92% methyl orange degradation under sunlight within 90 min for an optimized ternary composition with a 1:1:2 Zn:Ni:Cu molar ratio, with a performance that exceeded analogous binary mixtures [15]. Li *et al.* (2021) reported that a three-component $Ag_2MoO_4/Ag_2S/MoS_2$ photocatalyst achieved several-fold higher dye and antibiotic degradation rates than two-component combinations through efficient charge transfer across ternary interfaces [27]. A CuO-ZnO-NiO ternary nanocomposite thus represents a plausible high-efficiency photocatalyst platform for dye removal, as each oxide contributes complementary advantages within a unified heterojunction network.

In the CuO-ZnO-NiO ternary system under UV-A irradiation, band alignment between the n-type ZnO and the p-type CuO and NiO promotes spatial charge separation. ZnO acts as the primary photo-excited semiconductor under UV-A light. Owing to favourable conduction band alignment, photo-generated electrons in ZnO can migrate toward CuO, which functions as an electron-accepting component, thereby suppressing recombination. Meanwhile, NiO, as a p-type wide-band-gap oxide, facilitates hole transport and stabilization at the heterointerface. The directional migration of electrons and holes across different oxide domains enhances charge-carrier lifetime and strengthens the generation of reactive oxygen species during photocatalysis [15].

Light irradiation of a CuO-ZnO-NiO surface generates electron excitation from the valence band to the conduction band, and redox reactions on the catalyst surface then drive reactive oxygen species formation. Valence-band holes oxidise water molecules and hydroxide ions to produce hydroxyl radicals, while conduction-band electrons reduce dissolved oxygen to produce superoxide radicals (Fig. 1). The present work reports the structured development of a ternary CuO-ZnO-NiO nanocomposite for enhanced photocatalytic removal of DB15 from water, with a rationale that links ternary integration to a tailored band gap, broader light absorption, improved charge separation, and a higher specific surface area relative to single-oxide or binary-oxide systems. The study extends beyond previously reported ZnO-NiO, ZnO-CuO, and ZnO-NiO-CuO composites through a combined framework of green synthesis, adsorption-assisted photocatalysis, and ratio optimisation. *Ficus* leaf extract enabled green preparation of the CuO-ZnO-NiO system, adsorption was analysed as a complementary step that concentrates DB15 at reactive sites, and Cu:Zn:Ni screening identified 1:1:1 as the optimal composition for DB15 removal.

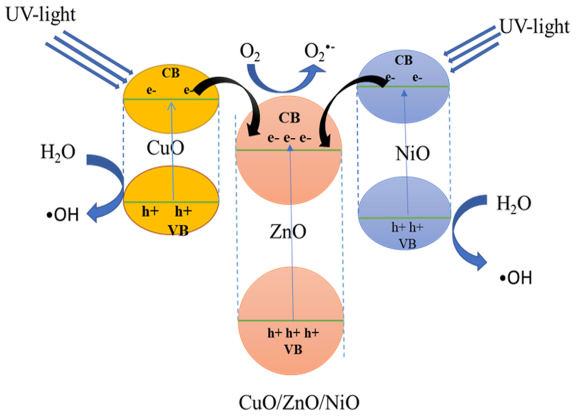

Fig. 1. Schematic illustration of the UV-induced photocatalytic mechanism of CuO-ZnO-NiO nanocomposites.

2. Materials and Methods

2.1. Reagents and chemicals

Analytical-grade chemicals (purity ≥99.9%) were used throughout the study. DB15 dye was obtained from Central Drug House (BDH, India). Copper(II) sulphate pentahydrate ($CuSO_4 \cdot 5H_2O$), nickel sulphate hexahydrate ($NiSO_4 \cdot 6H_2O$), and zinc sulphate heptahydrate ($ZnSO_4 \cdot 7H_2O$, >98%) served as metal precursors for CuO-ZnO-NiO nanocomposite preparation. Standard solutions of H_2SO_4 (1 M) and NaOH (1 M) were used to adjust solution pH during synthesis and during dye-removal experiments. A Shimadzu UV-1800 UV-Vis spectrophotometer measured DB15 absorbance for concentration tracking during adsorption and photocatalysis tests. Direct Blue 15 (Benzanil Sky Blue) is a dark blue powder dye. Its molecular formula is $C_{34}H_{24}N_6Na_4O_{16}S_4$, with a molecular weight of 992.8 g mol^{-1}. The compound is soluble in water and exhibits a maximum absorption wavelength (λmax) of 594 nm.

2.2. Preparation of Ficus leaf extract

Ficus leaves were collected in early summer 2025 from healthy, mature trees at the same location (University of Baghdad campus). Fully developed, disease-free leaves were selected to minimise environmental and physiological variability. Extract preparation followed a strictly standardised protocol,

and each synthesis series used freshly prepared extract. Comparable FTIR band positions and intensities, particularly hydroxyl and carbonyl bands, supported batch consistency across independent preparations. Consistent XRD patterns, crystallite size, and SEM morphology across independent syntheses supported product reproducibility.

Ficus leaves were thoroughly washed with tap water and rinsed with distilled water to remove impurities. The cleaned leaves were dried in a hot-air oven for 12 h at 50-60 °C to remove residual moisture. A fine powder was obtained after the dried leaves were ground. Leaf powder (40 g) was dispersed in deionised water (0.5 L) and heated at 85 ± 5 °C for 30 min. The mixture cooled to room temperature before filtration. Vacuum filtration removed suspended leaf residues and produced a clear extract. The filtrate was stored at 4 °C and served as a chelating and capping agent during nanocomposite synthesis. The extraction protocol followed [28] with minor modifications.

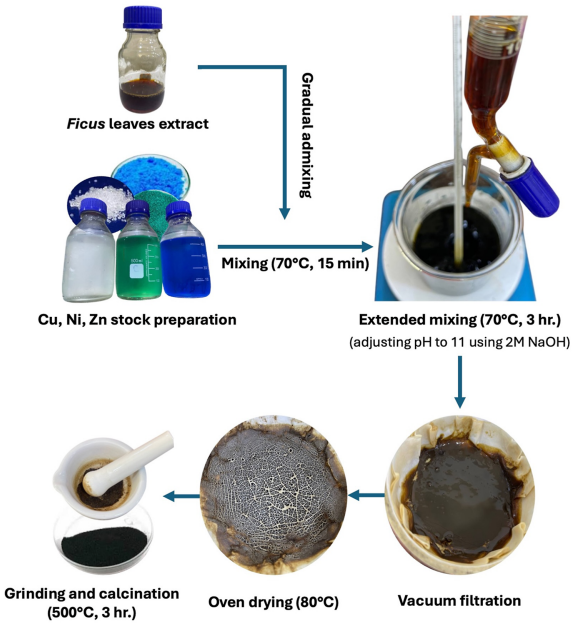

Fig. 2. Synthesis procedure for CuO-ZnO-NiO nanoparticles.

2.3. Preparation of CuO-ZnO-NiO nanocomposite photocatalysts

CuO-ZnO-NiO nanoparticle heterojunctions were synthesised by co-precipitation using $CuSO_4 \cdot 5H_2O$, $ZnSO_4 \cdot 7H_2O$, and $NiSO_4 \cdot 6H_2O$ as metal precursors. Four Cu:Zn:Ni molar ratios were prepared, namely 1:1:1 (1C:1Z:1N), 1:1:2 (1C:1Z:2N), 1:2:1 (1C:2Z:1N), and 2:1:1 (2C:1Z:1N), with precursor quantities listed in Table 1. Separate 0.2 M stock solutions of each metal salt were prepared in deionised water. Each solution was filtered through a 0.45 μm membrane.

A representative synthesis used the 2:1:1 composition (2C:1Z:1N). The precursor mixture was prepared by combining 50 mL of 0.2 M $CuSO_4 \cdot 5H_2O$, 25 mL of 0.2 M $ZnSO_4 \cdot 7H_2O$, and 25 mL of 0.2 M $NiSO_4 \cdot 6H_2O$. The mixed salt solution was stirred continuously for 15 min at 70 °C to ensure compositional homogeneity (Fig. 2). *Ficus* leaf extract (1.0 L) was added gradually to the stirred precursor mixture, and agitation was maintained at 70 °C to ensure uniform interaction between the phytochemicals and the metal ions. Sodium hydroxide (2 M) was then added dropwise until the suspension reached pH 11. The mixture was maintained under vigorous stirring and heating at 70 °C for 3 h to complete precipitation and composite formation. The precipitate was collected and washed four times with distilled water and three times with ethanol to remove residual salts and soluble impurities. The same procedure was applied to the remaining Cu:Zn:Ni ratios listed in Table 1.

2.4. Characterization methods

X-ray diffraction (XRD) using a Philips X'Pert diffractometer at Al-Nahrain University was used to identify crystalline phases and to assess the crystallographic structure of the CuO-ZnO-NiO nanocomposites. Fourier-transform infrared (FT-IR) spectroscopy using a Shimadzu IR Affinity-1 instrument was used to identify functional groups associated with surface chemistry and metal-oxygen bonding. Scanning electron microscopy (SEM) using a TESCAN VEGA 3 instrument was used to examine surface morphology and particle

Table 1. Molar proportions of $NiSO_4 \cdot 6H_2O$, $ZnSO_4 \cdot 7H_2O$, and $CuSO_4 \cdot 5H_2O$ used for synthesising CuO-ZnO-NiO heterojunction nanocomposites.

Salt composition (%)	Molar ratio of CuO-ZnO-NiO			
	2C:1Z:1N (2:1:1)	*1C:2Z:1N (1:2:1)*	*1C:1Z:2N (1:1:2)*	*1C:1Z:1N (1:1:1)*
$CuSO_4 . 5H_2O$	50	25	25	33.33
$ZnSO_4.6H_2O$	25	50	25	33.33
$NiSO_4.6H_2O$	25	25	50	33.33

aggregation. Transmission electron microscopy (TEM) was used to examine nanoscale morphology and particle-shape features. Atomic force microscopy (AFM) using a TT-2 instrument was used to examine surface topography and roughness via two- and three-dimensional maps. Brunauer-Emmett-Teller (BET) analysis using a TriStar II Plus system (Version 2.03) was used to determine specific surface area, pore volume, and pore-size distribution.

2.5. Analytical method

A calibration curve for DB15 was established at λ_{max} = 594 nm. DB15 concentrations during adsorption and photocatalysis experiments were determined from UV-Vis absorbance values using the calibration relationship. Removal efficiency (RE, %) was calculated according to Eq. (1):

$$RE\% = (C_0 - C_t) / C_0 \times 100 \quad (1)$$

C_t represents the instantaneous DB15 concentration at time t.

2.6. Batch UV-A photocatalysis

Batch photocatalysis experiments were conducted in a 1.0 L Pyrex beaker under magnetic stirring. Solution pH (3, 7, or 9) was adjusted before catalyst addition, and the suspension was stirred briefly to ensure uniform catalyst dispersion before irradiation. Aliquots were withdrawn at predefined intervals, filtered through a 0.45 μm membrane, and analysed by UV-Vis spectrophotometry at 594 nm. UV-A irradiation was provided by a semi-pilot photoreactor equipped with 24 UV-A lamps (8 W nominal power; peak wavelength 365 nm; 30 cm length; 2.2 cm diameter) fixed inside a cylindrical aluminium housing (40 cm diameter; 50 cm length) that provided reflective internal surfaces. A 10 cm lamp-to-reaction-cell distance and 2.3 cm lamp spacing were maintained. The reactor housing was mounted inside a 60 × 60 × 60 cm enclosure with air circulation, and the internal temperature remained within 30-40 °C under operation, with temperature monitoring via multiple thermocouples. UV intensity levels (6, 15, and 24 W m^{-2}) were reported as nominal values under the applied operating configuration; radiometric calibration with an external radiometer was not performed.

2.7. Batch adsorption procedure

Batch adsorption experiments evaluated DB15 uptake by CuO-ZnO-NiO nanocomposites with different Cu:Zn:Ni molar ratios. A catalyst dose of 0.5 g L^{-1} was dispersed in 1.0 L of DB15 solution (10 mg L^{-1}). Solution pH was adjusted to 6 before the adsorbent addition. Suspensions were agitated at 350 rpm for 180 min at room temperature to maintain uniform contact between dye molecules and adsorbent surfaces. Aliquots (10 mL) were collected at predefined time points and filtered through a 0.45 μm membrane to remove suspended solids. UV-Vis spectrophotometry (Shimadzu UV-1800) was used to record absorbance at λmax = 594 nm, and DB15 concentration was determined using the calibration procedure described in Section 2.4.

3. Results and Discussion

3.1. Characterization of CuO-ZnO-NiO NPs

FT-IR spectra of the calcined CuO-ZnO-NiO nanocomposites were recorded for all four Cu:Zn:Ni molar ratios over 400-4000 cm^{-1} (Fig. 3). Broad bands at 3545.16 and 3414 cm^{-1} indicate O-H stretching vibrations and suggest surface hydroxyl groups and adsorbed water. An absorption band at 873.75 cm^{-1} corresponds to aromatic C-C vibrations. Bands at 1473.62 and 1616.35 cm^{-1} correspond to C-O/C=O-related vibrations and indicate surface-adsorbed carbonyl-containing species on the nanocomposites. Low-wavenumber bands at 410.84 and 513.07 cm^{-1} appear in all compositions and fall within the metal-oxygen vibration region, which supports formation of the mixed-metal oxide framework. The FT-IR features agree with prior reports on related metal-oxide systems [29,30].

In the synthesis of transition metal oxides (i.e., CuO, ZnO, and NiO), the main chemical pathway involves hydroxide formation under alkaline conditions followed by dehydration to the

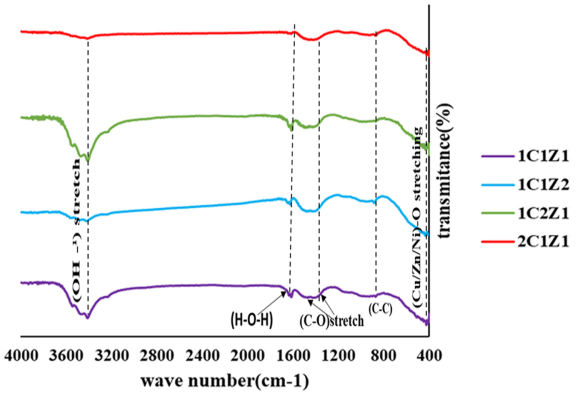

Fig. 3. FT-IR spectra of CuO-ZnO-NiO NCs prepared at four ratios.

corresponding oxides during thermal treatment. Plant extracts within this framework do not function solely as classical "reducing agents" in the sense of zero-valent metal reduction but rather influence multiple aspects of the precipitation and oxide formation process [31,32]. The complex mixture of phytochemicals present in *Ficus* leaf extract, which includes polyphenols, flavonoids, and compounds that bear carbonyl groups, can form coordination complexes with metal ions, which regulate nucleation, growth, and particle stabilization during precipitation and subsequent thermal conversion to oxides. Metal–phytochemical interactions help control particle size and morphology, suppress uncontrolled agglomeration, and act as chelating and capping agents that facilitate homogeneous nucleation and enhance colloidal stability.

SEM images illustrate the surface morphology of the CuO-ZnO-NiO nanocomposite (Fig. 4). SEM micrographs show aggregated particles with mixed rod-like and semi-spherical features and a heterogeneous spatial distribution. Particle size was estimated from SEM micrographs using ImageJ software (NIH, Bethesda, MD, USA). Particle-size values ranged from 36 to 83 nm, and the mean particle size reached 56.75 nm. Particle aggregation indicates interparticle contact and cluster formation, which can reduce the fraction of exposed surface sites available for dye adsorption and surface redox reactions [32].

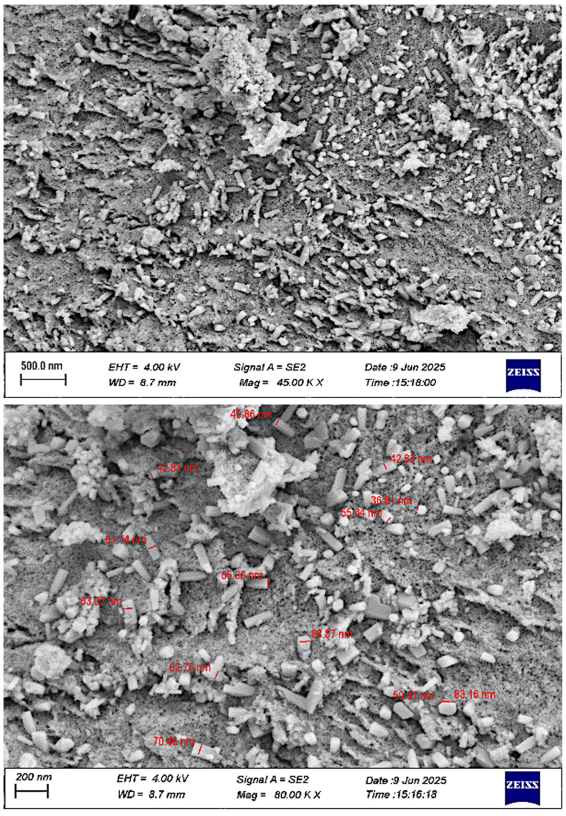

Fig. 4. SEM micrograph of CuO-ZnO-NiO nanoparticles.

AFM images show a nanoscale-textured surface for the CuO-ZnO-NiO nanocomposites (Fig. 5). AFM topography indicates a rough surface with granular features and a broadly distributed particle population across the scanned area. The average particle size reached 62.48 nm. Surface roughness can increase the number of accessible contact points between the dye solution and the nanocomposite surface, thereby supporting the adsorption of dye species during the initial uptake stage [33].

BET analysis yielded textural properties of the CuO-ZnO-NiO nanocomposites, including specific surface area, pore size, and pore volume. BET surface area calculations used the standard relative pressure range (P/P_0 = 0.05-0.30), which suits mesoporous materials. The reported BET surface area corresponds to the optimised CuO-ZnO-NiO composition (1:1:1). BET results indicate a specific surface area of 34.741 $m^2\ g^{-1}$, a total pore volume of 0.089 $cm^3\ g^{-1}$, and an average pore size of 10.299 nm. The average pore size of 10.299 nm falls within the mesoporous range (2-50 nm), which supports classification of the CuO-ZnO-NiO nanocomposites as mesoporous materials. Mesoporosity and higher surface area support photocatalysis by increasing the number of accessible surface sites and improving contact between reactants and catalyst surfaces during adsorption and surface reactions [34].

XRD patterns were recorded for CuO-ZnO-NiO nanocomposites prepared at Cu:Zn:Ni molar ratios of 1:1:1 (1C1Z1N), 1:1:2 (1C1Z2N), 1:2:1 (1C2Z1N), and 2:1:1 (2C1Z1N) (Fig. 6). Comparison with

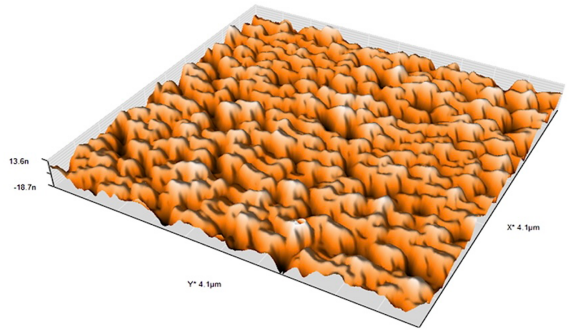

Fig. 5. AFM characterisation of CuO-ZnO-NiO NCs. Three-dimensional surface morphology image of the scanned area.

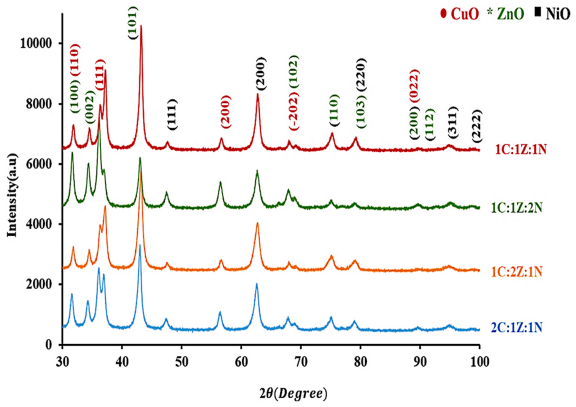

Fig. 6. XRD patterns of CuO-ZnO-NiO NCs prepared at Cu:Zn:Ni molar ratios of 1:1:1 (1C1Z1N), 1:1:2 (1C1Z2N), 1:2:1 (1C2Z1N), and 2:1:1 (2C1Z1N).

reference diffractograms from the JCPDS database supports phase identification and indicates consistent crystallographic features across compositions. All samples show similar major diffraction peaks, which indicates comparable crystal structures across the four ratios [15]. Peak matching supports the assignment of hexagonal wurtzite ZnO, cubic NiO, and monoclinic CuO and confirms the coexistence of three oxide phases within the CuO-ZnO-NiO nanocomposites [35].

The 1C1Z1N sample shows ZnO reflections at 2θ values of approximately 31.54°, 34.24°, 36.89°, 47.34°, 56.40°, and 67.78°, corresponding to the (100), (002), (101), (102), (110), and (112) planes, respectively. Agreement with JCPDS card No. 00-036-1451 supports ZnO phase assignment and indicates crystallographic consistency. CuO-related reflections appear at 2θ values of 24.91°, 66.17°, 68.89°, and 74.93°, which correspond to the indexed CuO planes reported in the manuscript. NiO-related reflections appear at 2θ values of 42.91°, 62.50°, and 78.90°, which correspond to the (200), (220), and (222) planes. The absence of unassigned peaks suggests high phase purity and indicates that no detectable secondary crystalline phases formed under the synthesis conditions. Three-phase coexistence, therefore, supports the successful formation of CuO-ZnO-NiO ternary nanocomposites. Prior reports on ZnO, CuO, and NiO nanostructures also commonly report phase coexistence rather than a single mixed phase in ternary oxide systems, and the present XRD results are consistent with these trends [36]. While phase identification was confirmed by comparison with JCPDS reference patterns, quantitative phase analysis using Rietveld refinement (a valuable technique for detailed microstructure characterization of metal

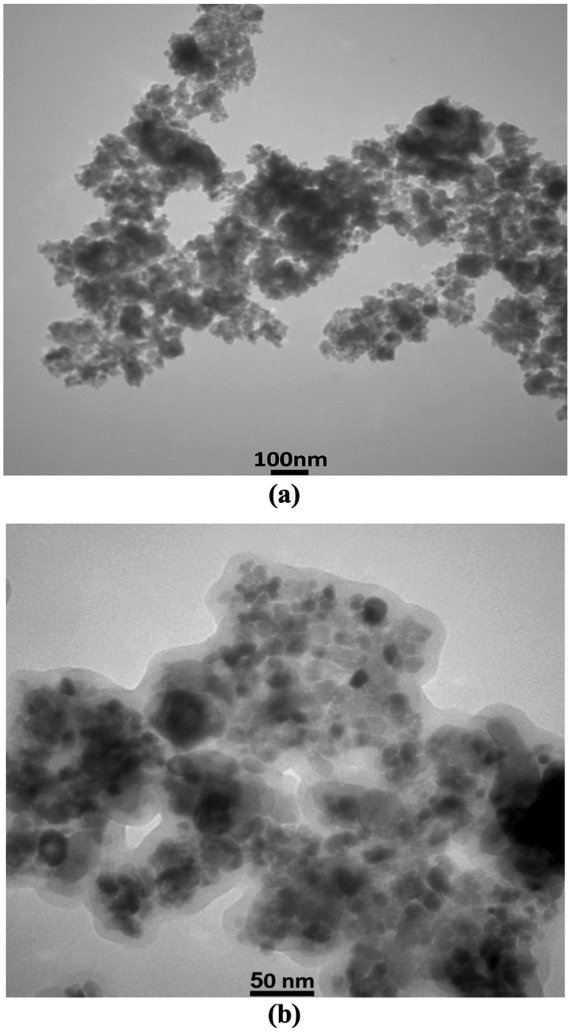

Fig. 7. TEM was employed to observe the optimised CuO-ZnO-NiO nanocomposite (1C:1Z:1N), which revealed its structural features at (a) 50 nm and (b) 100 nm scale bars.

oxide nanocrystals) represents an important direction for future work to determine precise phase fractions and crystallographic parameters for each Cu:Zn:Ni composition [37].

The 1:1:1 molar ratio CuO-ZnO-NiO nanocomposite (1C:1Z:1 N) was chosen for TEM characterisation because previous analyses showed superior physicochemical properties. TEM images at two different magnifications (Figs. 6a and 7b) revealed important structural features of the material. At lower magnification (Fig. 7a; scale bar: 50 nm), the nanoparticles exhibit a heterogeneous distribution with a tendency toward agglomeration, a common phenomenon in nanomaterials due to high surface energy. Particle size predominantly ranges from 20 to 40 nm, and the contrast variation observed suggests multilayered particle aggregation. The

nanoparticles display mostly spherical or quasi-spherical morphologies, which contribute to their structural stability. At higher magnification (Fig. 7b; scale bar: 100 nm), the image reveals a more open and well-dispersed arrangement of particles. The observed distribution suggests possible porosity within the nanocomposite, which supports improved performance in catalysis and environmental remediation processes [38]. Partial aggregation of the nanoclusters likely resulted from insufficient surface passivation or weak intermolecular interactions such as van der Waals forces. Reports describe CuO-ZnO nanocomposites with particle diameters of 15-35 nm and quasi-spherical morphologies [39]. Investigation of the ternary CuO-ZnO-NiO nanocomposite revealed spherical to quasi-spherical nanoparticles with sizes between 25 and 45 nm, along with evidence of particle agglomeration [15]. The observed morphology and particle size confirm successful nanoscale production of CuO-ZnO-NiO nanocomposites and agree with findings reported in the literature.

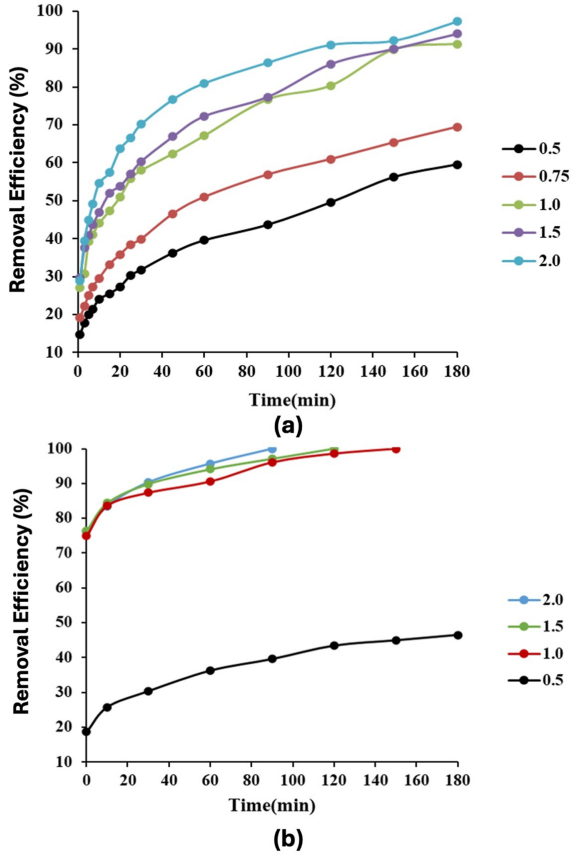

Fig. 8. Effect of CuO-ZnO-NiO NCs dose on DB15 removal: (a) adsorption at initial DB15 concentration 20 mg L^{-1}, pH 7, and 25 °C; (b) UV-A photocatalysis at initial DB15 concentration 30 mg L^{-1}, pH 3, and 35 °C.

3.2. Adsorption and photocatalytic performance

Adsorption experiments showed a monotonic increase in DB15 removal as nanocomposite dose increased from 0.5 to 2.0 g L^{-1}, with removal efficiencies of 59%, 69%, 91%, 93%, and 97%, respectively (Fig. 8). Photocatalysis experiments showed a similar dose dependence. A dose of 0.5 g L^{-1} achieved 46% removal after 180 min, whereas a dose of 1.0 g L^{-1} achieved complete degradation (100%) within 120 min. A dose of 1.5 g L^{-1} achieved complete degradation within 150 min, and a dose of 2.0 g L^{-1} achieved complete degradation within 90 min. A higher dose increases the number of available surface sites and strengthens contact between DB15 molecules and catalyst surfaces, which supports a higher adsorption uptake and higher photocatalytic rate [40]. A performance plateau emerged as dose increased from 1.5 to 2.0 g L^{-1} in the adsorption results, which indicates diminishing return once DB15 becomes the limiting species under the tested conditions. Higher catalyst loading can also promote aggregation and particle crowding, which reduce accessible surface area and introduce light-shielding during photocatalysis, thereby lowering the fraction of photoactive sites exposed to UV-A irradiation [41,42].

Solution pH affects catalyst surface charge, DB15 speciation in water, and reactive oxygen species formation under UV-A irradiation. DB15 removal was evaluated over pH 3–9, and removal efficiencies reached 89%, 74%, 76%, 73%, 91%, 67%, and 83% at pH 3, 4, 5, 6, 7, 8, and 9, respectively (Fig. 9a). Acidic conditions (pH 3-5) produced relatively high removal, and proton-rich media can increase the positive surface charge and strengthen electrostatic attraction to anionic dye species, which increases surface uptake [34]. Neutral conditions (pH 7) produced the highest removal (91%), and that outcome indicates a favourable balance between adsorption and oxidative removal capacity. Alkaline conditions reduced performance at pH 8 (67%), and increased negative surface charge can weaken adsorption through electrostatic repulsion with anionic dye species. Removal increased again at pH 9 (83%), and higher OH^- availability can promote hydroxyl radical formation and partially compensate for weaker adsorption [41].

Dark adsorption experiments were performed before irradiation to separate adsorption from photocatalytic degradation. Dark contact concentrated DB15 molecules on the nanocomposite surface through electrostatic attraction and surface complexation, and the measured removal in the dark represents adsorption-driven colour removal

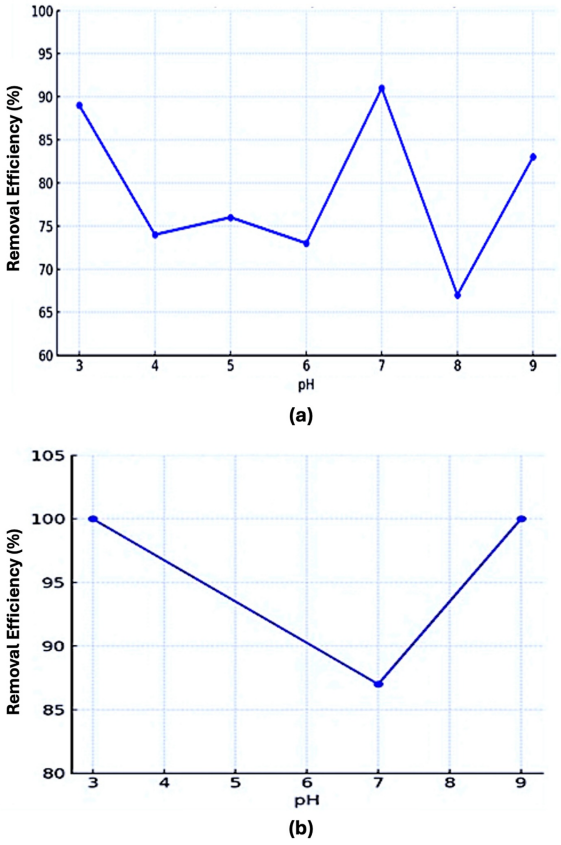

Fig. 9. Effect of initial pH on DB15 removal by CuO-ZnO-NiO NCs: (a) adsorption at NCs dose 1 g L^{-1}, initial DB15 concentration 20 mg L^{-1}, and 25 °C; (b) UV-A photocatalysis at nanocomposite dose 2 g L^{-1}, initial DB15 concentration 30 mg L^{-1}, 35 °C, and UV intensity 24 W m^{-2}.

rather than chemical degradation. UV-A irradiation then generated electron–hole pairs in the semiconductor phases, and interfacial charge transfer across the CuO-ZnO-NiO junctions reduced recombination and sustained reactive charge carriers at the surface. Surface reactions produced ·OH and $O_2\cdot^-$ radicals, and pre-adsorbed DB15 underwent rapid oxidation at or near the catalyst surface. Adsorption, therefore, reduced diffusion limitations by concentrating DB15 near reactive sites, thereby strengthening the apparent photocatalytic rate after illumination and explaining the rapid decline in concentration beyond adsorption equilibrium.

UV-A photocatalysis tests at pH 3, 7, and 9 show a strong pH dependence in both rate and final degradation. Photodegradation reached 100% within 90 min at pH 3, 87% after 180 min at pH 7, and 100% within 150 min at pH 9. Acidic conditions can accelerate degradation by promoting stronger dye adsorption onto a protonated surface and by enabling efficient radical-driven oxidation pathways under UV irradiation [43,44]. Neutral conditions produced slower degradation, which indicates weaker coupling between adsorption and radical-driven oxidation at pH 7 than at pH 3 or 9 [45]. Alkaline conditions achieved complete degradation, and OH^- availability can strengthen hydroxyl radical generation even when electrostatic repulsion reduces adsorption [41]. Acidic and alkaline media support complete DB15 photodegradation in the present system, while neutral pH favours adsorption-driven removal under the tested adsorption conditions.

To clearly distinguish between adsorption-driven colour removal and genuine photocatalytic degradation, all experiments were preceded by a dark equilibration step to establish adsorption-desorption equilibrium. The initial decrease in dye concentration observed in the dark corresponds to surface adsorption of dye molecules. Subsequent additional removal under UV-A irradiation is therefore attributed to photocatalytic degradation. While adsorption contributes to decolorization, the continued decline in concentration during irradiation indicates oxidative decomposition of the dye molecules rather than mere surface binding.

UV intensity affects photocatalytic DB15 degradation by controlling photon flux and, in turn, photogenerated electron-hole pair production at the catalyst surface. Fig. 10 shows higher DB15 degradation as UV intensity increased from 6 to 15 and 24 W m^{-2}. Degradation efficiencies reached 61%, 63%, and 67.7% at 6, 15, and 24 W m^{-2}, respectively. Higher photon flux can increase charge-carrier generation and accelerate radical-driven oxidation, which explains the observed performance increase with UV intensity. A UV intensity of 24 W m^{-2} was selected for subsequent

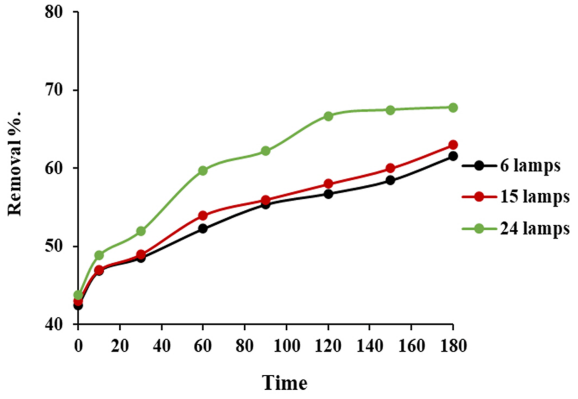

Fig. 10. Effect of UV intensity on DB15 photodegradation using CuO-ZnO-NiO NCs at catalyst dose 1 g L^{-1}, initial DB15 concentration 30 mg L^{-1}, pH 7, and 35 °C.

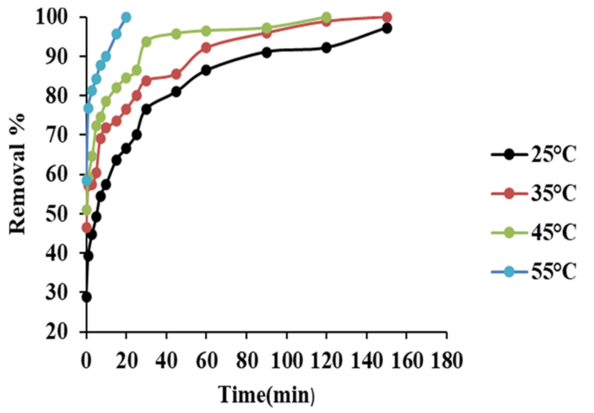

Fig. 11. Effect of temperature on DB15 removal using CuO-ZnO-NiO nanocomposites at catalyst dose 2.0 g L^{-1}, initial DB15 concentration 20 mg L^{-1}, and pH 7.

photocatalysis experiments as it produced the highest degradation under the tested conditions.

Temperature influences DB15 removal by affecting adsorption kinetics, dye diffusion in solution, and surface reaction rates. Adsorption experiments were performed from 25 to 55 °C, while other operating conditions remained constant. Fig. 11 shows an increase in DB15 removal from 97% at 25 °C to 100% at 55 °C. Higher temperature can increase dye-molecule mobility and enhance diffusion from the bulk solution to the nanocomposite surface, which can increase adsorption rate and support higher overall uptake under the tested contact time [46]. Higher temperatures can increase photocatalytic reaction rates and promote hydroxyl radical formation in semiconductor systems, which contribute to faster degradation under irradiation conditions.

Initial DB15 concentration influences removal by controlling the concentration gradient between the solution and nanocomposite surfaces and the ratio of available active sites to dye molecules. DB15 concentrations of 10, 20, 30, and 50 mg L^{-1} were evaluated under otherwise constant adsorption conditions. Fig. 12a shows complete removal at 10 mg L^{-1} within 45 min and complete removal at 20 mg L^{-1} within 150 min. Higher concentrations reduced removal at the same contact time, and removal reached 92% and 85% at 30 and 50 mg L^{-1}, respectively, after 180 min. Higher DB15 concentration increases competition for a fixed number of adsorption sites, which reduces the fraction of dye molecules removed at a given dose and contact time [47].

Photocatalysis experiments at DB15 concentrations of 30, 50, and 70 mg L^{-1} reached removal efficiencies of 100%, 85%, and 81%, respectively

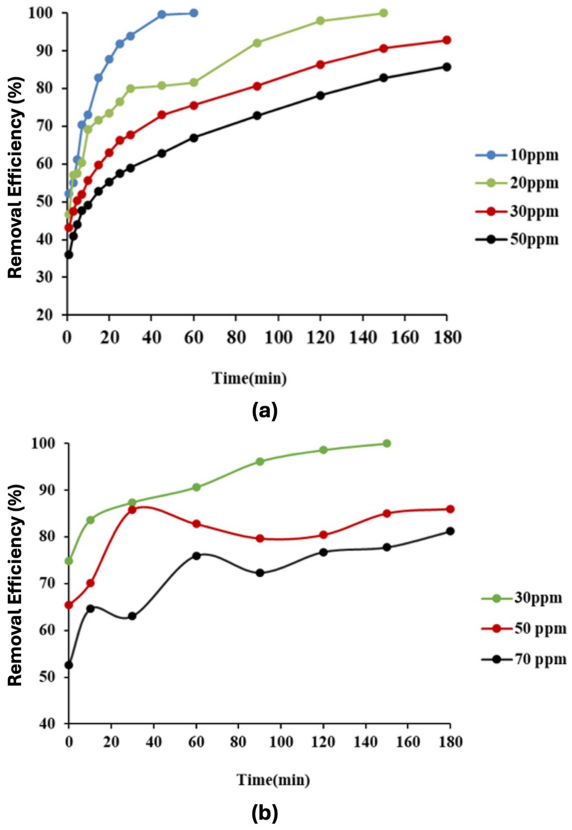

Fig. 12. Effect of initial DB15 concentration on (a) adsorption and (b) UV-A photocatalysis using CuO-ZnO-NiO nanocomposites. Adsorption conditions: NCs dose 2 g L^{-1} and pH 7. Photocatalysis conditions: NCs dose 1 g L^{-1}, pH 3, 35 °C, and UV intensity 24 W m^{-2}.

(Fig. 12b). Higher dye concentration increases UV attenuation through solution-phase absorbance, which reduces photon flux reaching catalyst surfaces and limits electron-hole generation and radical-driven oxidation [48], and reduces the fraction of available catalytic sites for oxidative reaction steps [49].

Dissolved salts can modify DB15 photodegradation by changing ionic strength, altering catalyst surface interactions, and introducing anions that participate in radical reactions. UV-A photodegradation of DB15 was evaluated in the presence of Na_2SO_4, Na_2CO_3, and NaCl (Fig. 13). Na_2SO_4 produced complete degradation (100%) within 30 min. Na_2CO_3 also produced complete degradation, but the reaction required 150 min. NaCl reduced performance, and degradation reached 80% after 180 min. Chloride ions can consume reactive radicals and form less reactive chlorine-containing species, which can reduce oxidative capacity and slow dye oxidation [50]. Carbonate ions can also react with hydroxyl radicals to slow degradation kinetics, even when

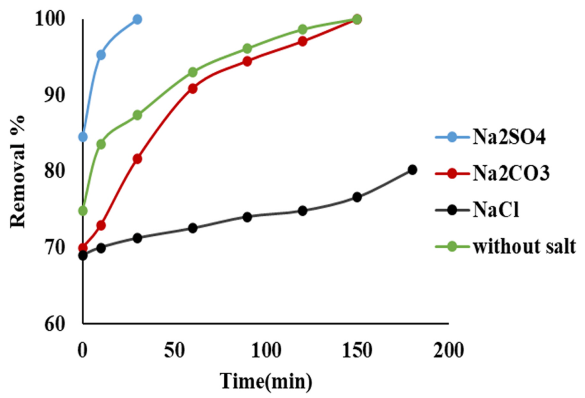

Fig. 13. Effect of salts on DB15 photodegradation using CuO-ZnO-NiO nanocomposites at nanocomposite dose 1.0 g L^{-1}, initial DB15 concentration 30 mg L^{-1}, salt concentration 1 M, pH 3, UV intensity 24 W m^{-2}, and 35 °C.

complete degradation occurs at longer reaction times. Sulfate-containing media, therefore, supported the fastest degradation under the tested conditions, whereas chloride-containing media produced the lowest degradation efficiency, and carbonate produced intermediate kinetics that depended on reaction time.

A 1.0 M salt concentration provided a high ionic-strength stress condition relevant to saline industrial wastewaters, such as textile dye-bath effluents. The selection, therefore, tested catalyst robustness under severe electrolyte load and clarified anion-specific effects on DB15 photodegradation.

To clearly differentiate between dye adsorption and true photocatalytic degradation, dark adsorption experiments were performed prior to light irradiation. The removal observed in the dark is solely due to dye adsorption on the catalyst surface and reflects color removal rather than chemical degradation. Under UV-A irradiation, however, a continuous decrease in dye concentration beyond the adsorption equilibrium was observed, confirming that photocatalytic degradation is the main mechanism responsible for effective dye removal.

The incorporation of CuO into the ZnO-NiO framework resulted in a noticeable red shift in the absorption edge, consistent with CuO's narrow band gap and its ability to absorb visible light [2]. The modification enhances spectral harvesting compared to binary or single-oxide systems. Nevertheless, although CuO extends optical absorption, the photocatalytic performance remains more pronounced under UV-A irradiation, indicating that the dominant activation pathway remains associated with the wide-band-gap components [51]. Therefore, in the present ternary system, CuO plays a dual role: partially extending light absorption into the visible region while more significantly promoting interfacial charge separation through heterojunction formation.

The enhanced photocatalytic performance of the ternary CuO-ZnO-NiO nanocomposite is consistent with improved charge separation facilitated by the formation of p-n heterojunctions at the interfaces between the three oxide phases. Similar ternary systems have attributed enhanced activity to this mechanism [15,38]. Future work employing photoluminescence spectroscopy and electrochemical impedance analysis would provide direct confirmation of reduced charge recombination in the green-synthesized material.

Despite the enhanced photocatalytic performance observed in this study, the dependence on UV-A irradiation limits its applicability to real wastewater treatment applications. UV-A accounts for only a small fraction of the solar spectrum, and large-scale implementation would require artificial UV sources, potentially increasing energy consumption and operational costs. Although incorporating CuO enhances partial visible-light absorption, the system remains predominantly UV-responsive due to the wide band gaps of ZnO and NiO. Therefore, further band-gap engineering and optimization toward visible-light activation are necessary to improve solar utilization efficiency and practical applicability in full-scale wastewater treatment systems.

3.3. Adsorption kinetics

Adsorption kinetics were evaluated using pseudo-first-order, pseudo-second-order, and Elovich models. Model-fitting quality indicates poor agreement with the Elovich model, as Elovich R^2 values were lower than those for the corresponding pseudo-first-order and pseudo-second-order fits. Pseudo-second-order provided the highest R^2 values across concentrations relative to pseudo-first-order, which indicates that pseudo-second-order kinetics describe DB15 uptake by CuO-ZnO-NiO nanocomposites more consistently under the present conditions.

Pseudo-first-order:

$$\log(q_e - q_t) = \log(q_e) - (k_1\, t)/2.303 \quad (2)$$

Pseudo-second-order:

$$t/q_t = 1/(k_2\, q_e^2) + t/q_e \quad (3)$$

Elovich:

$$q_t = (1/\beta)\ln(\alpha\beta) + (1/\beta)\ln(t) \quad (4)$$

Here, q_t denotes adsorption capacity at time t (mg g^{-1}) and q_e denotes equilibrium adsorption capacity (mg g^{-1}). k_1 denotes the pseudo-first-order rate constant (min^{-1}) and k_2 denotes the pseudo-second-order rate constant (g mg^{-1} min^{-1}). Parameter α denotes the initial adsorption rate (mg g^{-1} min^{-1}), and parameter β denotes the Elovich constant related to surface coverage and desorption behaviour (g mg^{-1}).

The pseudo-first-order model uses the linear form of log (q_e - q_t) versus time to obtain the rate constant k_1 and the equilibrium adsorption capacity q_e from the slope and intercept, respectively. The pseudo-second-order model uses the linear form of t/q_t versus time to obtain k_2 and q_e from the slope and intercept. The Elovich model is commonly applied to adsorption systems that involve heterogeneous surfaces and variable activation energies [52]. Elovich parameters α and β were obtained from the q_t versus ln(t) linear fit, where α represents the initial adsorption rate and β represents the desorption-related constant. Although the pseudo-second-order model fits the data well, it indicates adsorption-rate control rather than chemisorption, consistent with the low Dubinin-Radushkevich energy values, which confirm a physisorption-dominated mechanism.

Table 2 shows concentration-dependent changes in Elovich parameters. α increased and β decreased as initial DB15 concentration increased from 10 to 50 mg L^{-1}, which indicates faster initial uptake at higher driving concentration and slower desorption-related behaviour under the tested conditions.

3.4. Adsorption thermodynamics

DB15 adsorption onto CuO-ZnO-NiO nanocomposites was evaluated at 25, 35, 45, and 55 °C to determine adsorption spontaneity and temperature dependence. Standard thermodynamic parameters, including Gibbs free energy (ΔG°), enthalpy (ΔH°), and entropy (ΔS°), were derived using Eqs. (5)–(8) [53,54].

$$\Delta G^\circ = \Delta H^\circ - T\Delta S^\circ \quad (5)$$

$$\Delta G^\circ = -RT \ln Kc \quad (6)$$

The distribution constant (Kc) was defined as:

$$\ln Kc = \ln A - E_a/RT \quad (7)$$

$$Kc = q_e/C_e \quad (8)$$

A positive ΔH° (95.66 kJ mol^{-1}) indicates an endothermic adsorption process, and a positive ΔS° (353 J mol^{-1} K^{-1}) indicates increased randomness at the solid-liquid interface during adsorption.

3.5. Adsorption isotherms

Adsorption isotherms support quantitative evaluation of equilibrium uptake and adsorption capacity for DB15 on CuO-ZnO-NiO nanocomposites. The equilibrium data were analysed using the Langmuir, Freundlich, Temkin, and Dubinin-Radushkevich isotherm models (Eqs. 9-13) [55]. Table 3 reports the fitted parameters.

The Langmuir model estimates the maximum monolayer capacity (q_{max}) and the Langmuir constant (K_L) from the linear plot of $1/q_e$ versus $1/C_e$. The Langmuir separation factor (R_L) provides a criterion for adsorption favourability and follows Eq. (9). Adsorption shows favourable behaviour when R_L remains below 1, linear behaviour when R_L equals 1, and irreversible behaviour when R_L equals 0 [56].

Table 3. Isotherm parameters for DB15 adsorption onto CuO-ZnO-NiO NCs.

Isotherm model	Parameter	Value	R^2
Langmuir	q_{max} (mg g^{-1})	15.8	0.982
	K_L	63.2	
	R_L	0.0065-0.0013	
Freundlich	K_F	14.29	0.921
	1/n	0.174	
Temkin	K_T	1.98	0.922
	b_T (kJ mol^{-1})	0.13	
Dubinin-Radushkevich	q_m (mg g^{-1})	1.8	0.935
	β (mol^2 kJ^{-2})	2.85	
	E (kJ mol^{-1})	0.42	

Table 2. Adsorption kinetic parameters for DB15 adsorption onto CuO-ZnO-NiO NCs.

Initial DB15 concentration (mg L^{-1})	Pseudo-first Order		Pseudo-second Order		Elovich		
	k_1 (min^{-1})	R^2	k_2 (g mg^{-1} min^{-1})	R^2	α (mg g^{-1} min^{-1})	β (g mg^{-1})	R^2
10	0.0928	0.9549	0.157	0.9958	51.33	1.674	0.9064
20	0.0251	0.9532	0.784	0.9994	62.598	0.908	0.9732
30	0.0237	0.9864	0.331	0.9988	97.58	0.624	0.955
50	0.0214	0.9888	0.305	0.9985	144	0.536	0.9478

$$R_L = \frac{1}{1 + K_L C_0} \quad (9)$$

The Freundlich model estimates K_F and 1/n from the linear plot of log (q_e) versus log (C_e). Values of $0 < 1/n < 1$ reflect favourable adsorption on heterogeneous surfaces, whereas $1/n > 1$ reflects unfavourable adsorption under the tested conditions [57].

Langmuir:

$$\frac{1}{q_e} = \frac{1}{q_{max} K_L}\left(\frac{1}{C_e}\right) + \frac{1}{q_{max}} \quad (10)$$

Freundlich:

$$\log q_e = \left(\frac{1}{n}\right)\log C_e + \log K_F \quad (11)$$

Temkin:

$$q_e = B_T \ln C_e + B_T \ln K_T \quad (12)$$

Dubinin-Radushkevich:

$$\ln q_e = \ln q_m - \beta\epsilon^2 \quad (13)$$

Where q_e (mg g^{-1}) denotes adsorption capacity at equilibrium, C_e (mg L^{-1}) denotes equilibrium concentration, q_{max} (mg g^{-1}) denotes maximum monolayer capacity, and q_m (mg g^{-1}) denotes Dubinin-Radushkevich capacity. K_L, K_F, K_T, and β denote isotherm constants. Mean adsorption energy follows $E = (2\beta)^{-1/2}$. Parameter B_T follows $B_T = RT/b_T$, where R denotes the ideal gas constant (0.008314 kJ mol^{-1} K^{-1}) and T denotes absolute temperature (K). Parameter ϵ follows $\epsilon = RT \ln(1 + 1/C_e)$.

Isotherm fitting showed the highest correlation for the Langmuir model ($R^2 = 0.982$; Table 3), with $q_{max} = 15.8$ mg g^{-1} and $K_L = 63.2$. R_L values ranged from 0.0065 to 0.0013 across the studied initial DB15 concentrations, which supports favourable adsorption behaviour under the tested conditions [52]. The Freundlich model yielded KF = 14.29 and 1/n = 0.174, with a lower correlation ($R^2 = 0.921$), suggesting surface heterogeneity but providing a weaker fit than Langmuir [58]. The Temkin model yielded $K_T = 1.98$ and $b_T = 0.13$ kJ mol^{-1} with $R^2 = 0.922$, which supports a limited description of the equilibrium data relative to Langmuir. The Dubinin-Radushkevich model yielded $q_m = 1.8$ mg g^{-1}, $\beta = 2.85$ mol^2 kJ^{-2}, and E = 0.42 kJ mol^{-1} (420 J mol^{-1}), with $R^2 = 0.935$. Mean adsorption energy below 8 kJ mol^{-1} indicates physisorption, and the present E value indicates weak adsorbate-surface interactions under the tested conditions [59]. Langmuir fitting produced the highest correlation ($R^2 = 0.982$), so the Dubinin-Radushkevich model provides a supportive rather than a primary description of the equilibrium data. The Langmuir model, therefore, provides the most consistent description of the equilibrium uptake, which supports monolayer coverage of DB15 on CuO-ZnO-NiO nanocomposite surfaces.

3.6. Recycle test

CuO-ZnO-NiO nanocomposite reusability was evaluated over five consecutive cycles under identical conditions (pH 7, 35 °C, initial DB15 concentration 20 mg L^{-1}, and nanocomposite dose 2.0 g L^{-1}). After each cycle, the nanocomposite was separated from the treated solution, washed to remove loosely bound residues, dried, and then reused under the same operating conditions. Cycle 1 achieved 95% colour removal, followed by 93% and 91% in cycles 2 and 3. Cycles 4 and 5 showed a marked decline to 63% and 59%, respectively (Fig. 14). Surface fouling by strongly bound dye species or oxidation intermediates can reduce the number of accessible active sites and weaken interfacial charge transfer, which may explain the late-cycle efficiency loss. Catalyst aggregation and loss during recovery can also contribute to the drop in DB15 removal efficiency observed in cycles 4 and 5. Regeneration steps such as washing, drying, and mild reactivation can help maintain performance over repeated cycles [60].

Although the ternary CuO-ZnO-NiO catalyst maintained high photocatalytic activity during the first two reuse cycles, a noticeable reduction in removal efficiency was observed after the third cycle. This decline may be attributed to several factors, including the accumulation of refractory degradation intermediates on the catalyst surface, partial blockage of active sites, and mild particle aggregation during recovery and washing.

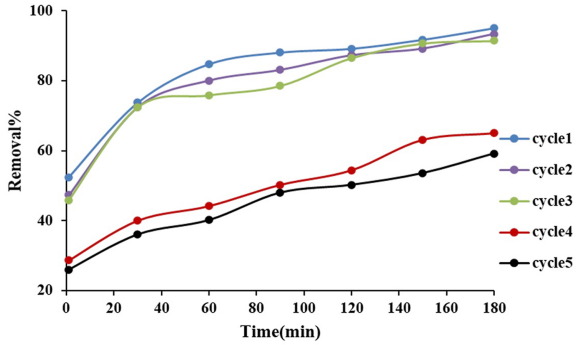

Fig. 14. Reusability of CuO-ZnO-NiO nanocomposite (1C:1Z:1 N) during DB15 removal across five cycles at pH 7, 35 °C, nanocomposite dose 2.0 g L^{-1}, and initial DB15 concentration 20 mg L^{-1}: removal efficiency per cycle.

Additionally, repeated irradiation may induce subtle surface chemical changes, particularly in Cu- and Ni-containing domains, which can influence interfacial charge-transfer efficiency. Importantly, post-reaction XRD patterns confirmed that the crystalline phases remained intact, indicating that the activity loss is more likely associated with surface deactivation rather than structural collapse. These findings suggest that while the catalyst exhibits reasonable short-term stability, further optimization is required to improve long-term durability for practical wastewater treatment applications.

The study evaluated DB15 removal under controlled laboratory conditions, and several limitations remain. The photocatalytic performance relies on UV-A irradiation, which limits direct translation to solar-driven treatment without additional optimization. UV-Vis monitoring confirms decolourisation and concentration decline, whereas the absence of TOC or COD measurements prevents confirmation of full mineralization. Catalyst stability assessment remains incomplete because post-use characterisation and metal-leaching quantification were not performed, and reuse data indicate possible activity loss that requires deeper analysis. Mechanistic interpretation relies on indirect evidence, and direct verification of charge separation and recombination trends will require techniques such as photoluminescence spectroscopy and electrochemical impedance analysis. The experimental matrix used model dye solutions and selected salts rather than real textile effluents with mixed organic and inorganic constituents, which limits generalisation to complex wastewater systems.

4. Conclusion

CuO-ZnO-NiO nanocomposites were successfully synthesized via a green co-precipitation method from *Ficus* leaf extract as a natural reducing and stabilizing agent for DB15 removal. The characterisation of the CuO-ZnO-NiO nanocomposites by FTIR, XRD, SEM, AFM, and BET confirmed crystalline and porous nanostructures, with a specific surface area of 34.74 $m^2 g^{-1}$ and a mean particle size of 56.75 nm. FTIR spectra revealed polyphenolic signatures supporting the role of plant-derived compounds in nanocomposite stabilization. The synthesized CuO-ZnO-NiO nanocomposites achieved effective DB15 removal through adsorption and UV-driven photocatalysis, with photocatalysis reaching complete dye removal (100%) and adsorption achieving 92% under optimal conditions. The 1:1:1 (1C1Z1N) composition produced the strongest overall performance among the tested molar ratios. Reuse tests showed removal efficiency above 90% across three cycles, followed by 63% and 59% in cycles four and five, indicating partial deactivation during repeated operation. Thermodynamic and kinetic analyses indicated endothermic physisorption, and the pseudo-second-order model best described the adsorption data. While the decrease in characteristic absorption peaks indicates effective chromophore degradation, UV-Vis analysis alone does not confirm complete mineralization to CO_2 and H_2O. In the absence of total organic carbon (TOC) or chemical oxygen demand (COD) measurements, the results should be interpreted as photocatalytic degradation rather than full mineralization. Future studies will include TOC analysis to provide a more comprehensive assessment of mineralization efficiency. CuO-ZnO-NiO nanocomposites synthesized via *Ficus* leaf extract, therefore, represent recyclable and environmentally compatible materials for dye-contaminated wastewater treatment.

Ethics information

Ethics approval was not required for this study because it did not involve human participants or animals.

Funding

This work received no funding.

Conflict of interest

The authors declare that they have no competing interests.

Acknowledgements

The authors thank the Department of Biochemical Engineering, Al-Khwarizmi College of Engineering, University of Baghdad, Iraq, for access to laboratory facilities and instrumentation.

References

[1] L. Lin, H. Yang, X. Xu, Effects of water pollution on human health and disease heterogeneity: a review, Front. Environ. Sci. 10 (2022) 880246, https://doi.org/10.3389/fenvs.2022.880246.
[2] M.A. Ahmed, S.A. Mahmoud, A.A. Mohamed, Interfacially engineered metal oxide nanocomposites for enhanced photocatalytic degradation of pollutants and energy applications, RSC Adv. 15 (2025) 15561–15603, https://doi.org/10.1039/D4RA08780A.
[3] M.E. El Awady, F.N. El-Shall, G.E. Mohamed, A.M. Abd-Elaziz, M.O. Abdel-Monem, M.G. Hassan, Exploring the

decolorization efficiency and biodegradation mechanisms of different functional textile azo dyes by Streptomyces albidoflavus 3MGH, BMC Microbiol. 24 (2024) 210, https://doi.org/10.1186/s12866-024-03347-9.
[4] M. Kumar, A. Mishra, S.K. Patel, J. Kushwaha, S. Singh, V. Mishra, D. Singh, V. Singh, B.S. Giri, R.R. Singhania, D. Singh, Environmental impacts and strategies for bioremediation of dye-containing wastewater, Bioengineering 12 (2025) 1043, https://doi.org/10.3390/bioengineering12101043.
[5] M. Hernández-Zamora, F. Martínez-Jerónimo, Exposure to the Azo dye direct blue 15 produces toxic effects on microalgae, cladocerans, and zebrafish embryos, Ecotoxicology 28 (2019) 890–902, https://doi.org/10.1007/s10646-019-02087-1.
[6] M.A. Iqbal, S. Akram, S. Khalid, B. Lal, S.U. Hassan, R. Ashraf, G. Kezembayeva, M. Mushtaq, N. Chinibayeva, A. Hosseini-Bandegharaei, Advanced photocatalysis as a viable and sustainable wastewater treatment process: a comprehensive review, Environ. Res. 253 (2024) 118947, https://doi.org/10.1016/j.envres.2024.118947.
[7] M. Kurnia, S. Suprapto, Y.L. Ni'mah, Bio-adsorbent for remazol Brilliant Blue R (RBBR) dye, S. Afr. J. Chem. Eng. 47 (2024) 111–122, https://doi.org/10.1016/j.sajce.2023.11.002.
[8] M.A. Ahmed, A.A. Mohamed, Advances in ultrasound-assisted synthesis of photocatalysts and sonophotocatalytic processes: a review, iScience 27 (2024) 108583, https://doi.org/10.1016/j.isci.2023.108583.
[9] A. Amin, R.N. Kim, J. Kim, W.D. Kim, Recent breakthroughs in overcoming the efficiency limits of photocatalysis for hydrogen generation, Catalysts 15 (2025) 1067, https://doi.org/10.3390/catal15111067.
[10] M.G. Lines, Nanomaterials for practical functional uses, J. Alloys Compd. 449 (2008) 242–245, https://doi.org/10.1016/j.jallcom.2006.02.082.
[11] C.B. Ong, L.Y. Ng, A.W. Mohammad, A review of ZnO nanoparticles as solar photocatalysts: Synthesis, mechanisms and applications, Renew. Sustain. Energy Rev. 81 (2018) 536–551, https://doi.org/10.1016/j.rser.2017.08.020.
[12] A. Mishra, A. Mehta, S. Basu, Clay supported TiO_2 nanoparticles for photocatalytic degradation of environmental pollutants: a review, J. Environ. Chem. Eng. 6 (2018) 6088–6107, https://doi.org/10.1016/j.jece.2018.09.029.
[13] S.M. Jassim, M.A. Abd, I.A. Hammed, Green synthesis of nickel oxide nanoparticles using syzygium aromatic extract: characterization and biological applications, Al-Bahir. 2 (2023) 7, https://doi.org/10.55810/2313-0083.1024.
[14] A.K. Sibhatu, G.K. Weldegebrieal, S. Sagadevan, N.N. Tran, V. Hessel, Photocatalytic activity of CuO nanoparticles for organic and inorganic pollutants removal in wastewater remediation, Chemosphere 300 (2022) 134623, https://doi.org/10.1016/j.chemosphere.2022.134623.
[15] M.Z. Ishaque, M. Abid, F. Naz, A. Kanwal, M.K. Ullah, U. Aftab, Fabrication of ternary metal oxide (ZnO:NiO:CuO) nanocomposite heterojunctions for enhanced photocatalytic and antibacterial applications, RSC Adv. 13 (2023) 30838–30854, https://doi.org/10.1039/D3RA05170F.
[16] S. Saravanan, R.S. Dubey, Optical and structural investigations of TiO_2 multilayers on glass prepared via sol-gel spin-coating technique, Mater. Today Proc. 49 (2022) 2872–2875, https://doi.org/10.1016/j.matpr.2021.10.129.
[17] P. Panchal, D.R. Paul, A. Sharma, D. Hooda, R. Yadav, P. Meena, S.P. Nehra, Phytoextract mediated ZnO/MgO nanocomposites for photocatalytic and antibacterial activities, J. Photochem. Photobiol. Chem. 385 (2019) 112049, https://doi.org/10.1016/j.jphotochem.2019.112049.
[18] L.M. Anaya-Esparza, E. Montalvo-González, N. González-Silva, M.D. Méndez-Robles, R. Romero-Toledo, E.M. Yahia, A. Pérez-Larios, Synthesis and characterization of TiO_2-ZnO-MgO mixed oxide and their antibacterial activity, Materials 12 (2019) 698, https://doi.org/10.3390/ma12050698.
[19] J. Cai, H. Tao, Y. Peng, X. Zhao, P. Hu, Y. Zhou, H. Lyu, Y. Gao, S. Guo, Enhanced charge separation of NiO/ZnO p-n heterojunction nanorod arrays for photoelectrochemical water splitting, Surf. Interfaces. 55 (2024) 105376, https://doi.org/10.1016/j.surfin.2024.105376.
[20] J.F. de Brito, F. Tavella, C. Genovese, C. Ampelli, M.V.B. Zanoni, G. Centi, S. Perathoner, Role of CuO in the modification of the photocatalytic water splitting behaviour of TiO_2 nanotube thin films, Appl. Catal. B Environ. 224 (2018) 136–145, https://doi.org/10.1016/j.apcatb.2017.09.071.
[21] W. Lu, T. Gu, X. Jing, Y. Zhu, L. Yu, S. Hou, T. Pang, N. Lu, Z. Zhang, Ag nanoparticles-decorated p-Type CuO/n-Type ZnO heterojunction nanofibers with enhanced photocatalytic activities for dye degradation and disinfection, J. Alloys Compd. 968 (2023) 171864, https://doi.org/10.1016/j.jallcom.2023.171864.
[22] C. Aivalioti, E.G. Manidakis, N.T. Pelekanos, M. Androulidaki, K. Tsagaraki, Z. Viskadourakis, E. Spanakis, E. Aperathitis, Niobium-doped NiO as p-Type nanostructured layer for transparent photovoltaics, Thin Solid Films 778 (2023) 139910, https://doi.org/10.1016/j.tsf.2023.139910.
[23] K. Zhu, G. Mul, A. Huijser, Dye-sensitized NiO photocathodes: research progress, current mechanistic understanding, and research perspectives, Chem. Phys. Rev. 5 (2024) 021305, https://doi.org/10.1063/5.0170022.
[24] Z. Chen, T. Dedova, N. Spalatu, N. Maticiuc, M. Rusu, A. Katerski, I. Oja Acik, T. Unold, M. Krunks, ZnO/NiO heterostructures with enhanced photocatalytic activity obtained by ultrasonic spraying of a NiO shell onto ZnO nanorods, Colloids Surf. A Physicochem. Eng. Asp. 648 (2022) 129366, https://doi.org/10.1016/j.colsurfa.2022.129366.
[25] M.A. Ameya, N.B. Bekela, J.N. Guyasa, K. Zhu, T.T. Beyene, Enhanced photocatalytic and antibacterial performance of ZnO/CuO nanocomposites via carbon dot decoration, J. Mater. Sci. Mater. Electron. 20 (2025) 138, https://doi.org/10.1186/s40712-025-00350-4.
[26] A.G. Bekru, L.T. Tufa, O.A. Zelekew, M. Goddati, J. Lee, F. K. Sabir, Green synthesis of a CuO-ZnO nanocomposite for efficient photodegradation of methylene blue and reduction of 4-Nitrophenol, ACS Omega 7 (2022) 30908–30919, https://doi.org/10.1021/acsomega.2c02687.
[27] L. Li, D. Yin, L. Deng, S. Xiao, Y. Ouyan, K.K. Khaing, X. Guo, J. Wang, Z. Luo, Fabrication of a novel ternary heterojunction composite Ag2MoO4/Ag2S/MoS2 with significantly enhanced photocatalytic performance, New J. Chem. 45 (2021) 223–234, https://doi.org/10.1039/D0NJ04290K.
[28] H.M. Abdel-Aziz, R.S. Farag, S.A. Abdel-Gawad, Carbamazepine removal from aqueous solution by green synthesis zero-valent Iron/Cu nanoparticles with Ficus benjamina leaves' extract, Int. J. Environ. Res. 13 (2019) 843–852, https://doi.org/10.1007/s41742-019-00220-w.
[29] A.G. Ramu, M.L.A. Kumari, M.S. Elshikh, H.H. Alkhamis, A. F. Alrefaei, D. Choi, A facile and green synthesis of CuO/NiO nanoparticles and their removal activity of toxic nitro compounds in aqueous medium, Chemosphere 271 (2021) 129475, https://doi.org/10.1016/j.chemosphere.2020.129475.
[30] D. Dodoo-Arhin, T. Asiedu, B. Agyei-Tuffour, E. Nyankson, D. Obada, J.M. Mwabora, Photocatalytic degradation of rhodamine dyes using zinc oxide nanoparticles, Mater. Today Proc. 38 (2021) 809–815, https://doi.org/10.1016/j.matpr.2020.04.597.
[31] I.J. Lithi, K.I.A. Nakib, A.M.S. Chowdhury, M.S. Hossain, A review on the green synthesis of metal (Ag, Cu, and Au) and metal oxide (ZnO, MgO, Co 3 O 4, and TiO 2) nanoparticles using plant extracts for developing antimicrobial properties, Nanoscale Adv. 7 (2025) 2446–2473, https://doi.org/10.1039/D5NA00037H.
[32] S. Balaji, M.S. Pandian, R. Ganesamoorthy, T. Karchiyappan, Green synthesis of metal oxide nanoparticles using plant extracts: a sustainable approach to combat antimicrobial resistance, Environ. Nanotechnol. Monit. Manag. 23 (2025) 101066, https://doi.org/10.1016/j.enmm.2025.101066.
[33] M. Solís-López, A. Durán-Moreno, F. Rigas, A.A. Morales, M. Navarrete, R.M. Ramírez-Zamora, Assessment of copper slag as a sustainable fenton-type photocatalyst for water disinfection, in: S. Ahuja, eds., Water Reclamation and

Sustainability, Elsevier. 2014, pp. 199–227, https://doi.org/10.1016/B978-0-12-411645-0.00009-2.
[34] J. Wang, J. Tang, Fe-Based fenton-like catalysts for water treatment: preparation, characterization and modification, Chemosphere 276 (2021) 130177, https://doi.org/10.1016/j.chemosphere.2021.130177.
[35] M. Rezaei, A. Nezamzadeh-Ejhieha, The ZnO-NiO nanocomposite: a brief characterization, kinetic and thermodynamic study and study the arrhenius model on the sulfasalazine photodegradation, Int. J. Hydrogen Energy 45 (2020) 24749–24764, https://doi.org/10.1016/j.ijhydene.2020.06.258.
[36] H. Premkumar, S. Vadivel, H. Al-Lohedan, S.R.M. Syed, Synthesis and characterization of ternary ZnO/CuO/NiO nanocomposite for pseudocapacitive energy storage application, Vacuum 241 (2025) 114650, https://doi.org/10.1016/j.vacuum.2025.114650.
[37] J.A. Ramos-Guivar, J.C. Gonzalez-Gonzalez, F.J. Litterst, E. C. Passamani, Rietveld refinement, μ-Raman, X-ray photoelectron, and Mössbauer studies of metal oxide-nanoparticles growth on multiwall carbon nanotubes and graphene oxide, Cryst. Growth Des. 21 (2021) 2128–2141, https://doi.org/10.1021/acs.cgd.0c01551.
[38] A.O. Juma, E.A.A. Arbab, C.M. Muiva, L.M. Lepodise, G.T. Mola, Synthesis and characterization of cuo-nio-zno mixed metal oxide nanocomposite, J. Alloys Compd. 723 (2017) 866–872, https://doi.org/10.1016/j.jallcom.2017.06.288.
[39] A. Melese, W. Wubet, A. Abebe, A. Hussen, A comprehensive review on recent progress in synthesis methods of ZnO/CuO nanocomposites and their biological and photocatalytic applications, results, Chem 14 (2025) 102141, https://doi.org/10.1016/j.rechem.2025.102141.
[40] I.A.W. Tan, A.L. Ahmad, B.H. Hameed, Adsorption of basic dye on high-surface-area activated carbon prepared from coconut husk: equilibrium, kinetic and thermodynamic studies, J. Hazard. Mater. 154 (2008) 337–346, https://doi.org/10.1016/j.jhazmat.2007.10.031.
[41] N. Daneshvar, D. Salari, A.R. Khataee, Photocatalytic degradation of Azo Dye acid red 14 in water on ZnO as an alternative catalyst to TiO_2, J. Photochem. Photobiol. Chem. 162 (2004) 317–322, https://doi.org/10.1016/S1010-6030(03)00378-2.
[42] G. Crini, E. Lichtfouse, Advantages and disadvantages of techniques used for wastewater treatment, Environ. Chem. Lett. 17 (2019) 145–155, https://doi.org/10.1007/s10311-018-0785-9.
[43] M.A. Rauf, S.S. Ashraf, Fundamental principles and application of heterogeneous photocatalytic degradation of dyes in solution, Chem. Eng. J. 151 (2009) 10–18, https://doi.org/10.1016/j.cej.2009.02.026.
[44] S. Ahmed, M.G. Rasul, W.N. Martens, R. Brown, M.A. Hashib, Advances in heterogeneous photocatalytic degradation of phenols and dyes in wastewater: a review, Water Air Soil Pollut. 215 (2011) 3–29, https://doi.org/10.1007/s11270-010-0456-3.
[45] Y. Qi, D. Szendrak, R.T.W. Yuen, A.F.A. Hoadley, G. Mudd, Application of sludge dewatered products to soil and its effects on the leaching behaviour of heavy metals, Chem. Eng. J. 166 (2011) 586–595, https://doi.org/10.1016/j.cej.2010.11.029.
[46] K. Kobayashi, Y. Hashimoto, S.-L. Wang, Boron incorporation into precipitated calcium carbonates affected by aqueous pH and boron concentration, J. Hazard. Mater. 383 (2020) 121183, https://doi.org/10.1016/j.jhazmat.2019.121183.
[47] M.N. Chong, B. Jin, C.W.K. Chow, C. Saint, Recent developments in photocatalytic water treatment technology: a review, Water Res. 44 (2010) 2997–3027, https://doi.org/10.1016/j.watres.2010.02.039.
[48] M.N. Zafar, Q. Dar, F. Nawaz, M.N. Zafar, M. Iqbal, M.F. Nazar, Effective adsorptive removal of azo dyes over spherical ZnO nanoparticles, J. Mater. Res. Technol. 8 (2019) 713–725, https://doi.org/10.1016/j.jmrt.2018.06.002.
[49] I.M. Rashid, S.D. Salman, A.K. Mohammed, Y.S. Mahdi, Green synthesis of nickel oxide nanoparticles for adsorption of dyes, Sains Malays. 51 (2022) 533–546, https://doi.org/10.17576/jsm-2022-5102-17.
[50] K.A. Sukkar, A.A. Karamalluh, T.N. Jaber, Rheological and thermal properties of lubricating oil enhanced by the effect of CuO and TiO_2 nano-additives, Al-Khwarizmi Eng. J. 15 (2019) 24–33, https://doi.org/10.22153/kej.2019.12.002.
[51] D.H. Ramakrishnegowda, S.C. Kampalapura, D. Urs, M. Elfeky, J. Krishnegowda, S. Rangappa, K.S. Rangappa, S. Shivanna, Synthesis of p-CuO/n-ZnO heterostructure by microwave hydrothermal method and evaluation of its photo and bio-catalytic performance, Heliyon 9 (2023) e22758, https://doi.org/10.1016/j.heliyon.2023.e22758.
[52] J.R.F.G. de Carvalho, J.M.P.Q. Delgado, Lateral dispersion in liquid flow through packed beds at $Pe_m < 1{,}400$, AIChE J. 46 (2000) 1089–1095, https://doi.org/10.1002/aic.690460520.
[53] F.-C. Wu, R.-L. Tseng, R.-S. Juang, Characteristics of elovich equation used for the analysis of adsorption kinetics in dye-chitosan systems, Chem. Eng. J. 150 (2009) 366–373, https://doi.org/10.1016/j.cej.2009.01.014.
[54] S. Raghav, D. Kumar, Adsorption equilibrium, kinetics, and thermodynamic studies of fluoride adsorbed by tetrametallic oxide adsorbent, J. Chem. Eng. Data 63 (2018) 1682–1697, https://doi.org/10.1021/acs.jced.8b00024.
[55] A.A. Mohammed, T.J. Al-Musawi, S.L. Kareem, M. Zarrabi, A.M. Al-Ma'abreh, Simultaneous adsorption of tetracycline, amoxicillin, and ciprofloxacin by pistachio shell powder coated with zinc oxide nanoparticles, Arab. J. Chem. 13 (2020) 4629–4643, https://doi.org/10.1016/j.arabjc.2019.10.010.
[56] E. Derakhshani, A. Naghizadeh, M. Khodadadi, Application of different isotherm models for humic acid adsorption onto bentonite and montmorillonite nanoparticles, Health Scope 6 (2016) 40416, https://doi.org/10.5812/jhealthscope.40416.
[57] K.M. Al-Qahtani, Cadmium removal from aqueous solution by green synthesis zero-valent silver nanoparticles with benjamina leaves extract, Egypt, J. Aquat. Res. 43 (2017) 269–274, https://doi.org/10.1016/j.ejar.2017.10.003.
[58] R. Sivaranjanee, P.S. Kumar, S. Mahalaxmi, A review on agro-based materials for the separation of environmental pollutants from water system, Chem. Eng. Res. Des. 181 (2022) 423–457, https://doi.org/10.1016/j.cherd.2022.04.002.
[59] Y. Chen, Y. Zhu, Z. Wang, Y. Li, L. Wang, L. Ding, X. Gao, Y. Ma, Y. Guo, Application studies of activated carbon derived from rice husks produced by chemical-thermal process: a review, Adv. Colloid Interface Sci. 163 (2011) 39–52, https://doi.org/10.1016/j.cis.2011.01.006.
[60] Q.U. Khan, N. Begum, Z.U. Rehman, A.U. Khan, K. Tahir, E. M. El-Din, A.A. Alothman, M.A. Habila, D. Liu, P. Bocchetta, M.S. Javed, Development of efficient and recyclable ZnO-CuO/g-C_3N_4 nanocomposite for enhanced adsorption of arsenic from wastewater, Nanomaterials 12 (2022) 3984, https://doi.org/10.3390/nano12223984.